Supporting Information for

Morphological and optical properties of carbonaceous aerosol particles from ship emissions and biomass burning during a summer cruise measurement in the South China Sea

Cuizhi Sun[1], Yongyun Zhang[1], Baoling Liang[1,&], Min Gao[1], Xi Sun[1,#], Fei Li[1,4], Xue Ni[1], Qibin Sun[1], Hengjia Ou[1], Dexian Chen[1], Shengzhen Zhou[1,2,3*], and Jun Zhao[1,2,3*]

[1] School of Atmospheric Sciences, Guangdong Province Key Laboratory for Climate Change and Natural Disaster Studies, and Southern Marine Science and Engineering Guangdong Laboratory (Zhuhai), Sun Yat-sen University, Zhuhai, Guangdong 519082, China

[2] Guangdong Provincial Observation and Research Station for Climate Environment and Air Quality Change in the Pearl River Estuary, Zhuhai, Guangdong 519082, China

[3] Key Laboratory of Tropical Atmosphere-Ocean System, Ministry of Education, Zhuhai, Guangdong 519082, China

[4] Xiamen Key Laboratory of Straits Meteorology, Xiamen Meteorological Bureau, Xiamen, Fujian 361012, China

[&] Now at Guangzhou Environmental Monitoring Center, Guangzhou, Guangdong 510060, China

[#] Now at Centre for Isotope Research (CIO), Energy and Sustainability Research Institute Groningen (ESRIG), University of Groningen, Groningen 9747 AG, the Netherlands

Correspondence to: Jun Zhao (zhaojun23@mail.sysu.edu.cn) and Shengzhen Zhou (zhoushzh3@mail.sysu.edu.cn)

This supplement contains 12 sections, 1 table, and 16 figures.

1. Calculation of the cut size diameter of the TEM sampler

A single-stage cascade impactor, equipped with a jet nozzle of 0.3 mm in diameter, was used for single particle sampling. The Stokes number is defined in Eqs. (1–2) (Marple and Olson, 2011). The cut-size diameter, which is defined as the diameter corresponding to a 50% collection efficiency, can be derived using Eq. (3).

$$Stk = \frac{\rho_p C_c d_p^2 U}{9\eta W} \tag{1}$$

$$U = \frac{Q}{\pi(\frac{W}{2})^2} \tag{2}$$

$$d_{p_{50}} = \sqrt{Stk_{50}}\sqrt{\frac{9\eta\pi W^3}{4\rho_p C_c Q}} \tag{3}$$

where Stk is Stokes number, and the square root of the Stk corresponding to 50% collection efficiency ($\sqrt{Stk_{50}}$) is 0.47 assumed a jet Reynolds number of 3000; ρ_p is particle density assumed as 1.5 g cm^{-3}; C_c is Cunningham's slip correction factor, approximately 1; η is air (or gas) viscosity, 1.8134×10^{-5} Pa·s at 293 K, a constant under normal atmospheric condition. U represents the average air (or gas) velocity at the nozzle exit; Q is the volumetric flow rate through the nozzle and is equal to 1 L min^{-1}; W is the nozzle diameter and is 0.3 mm; $d_{p_{50}}$ is the cut point particle diameter at the 50% collection efficiency.

2. Single particle analysis using the ImageJ's plugin

Figure S1 shows examples of TEM images using the software program ImageJ for single particle analysis. Figure S1a is captured before beam focus, which is subsequently used for single particle analysis in Figure S1b. However, particles No. 2 and No. 13 (indicated by the red arrow) were manually excluded from the statistical analysis due to overcounting. In Figure S1c, volatile components were vaporized after beam focus, leaving nonvolatile compositions such as BC residual on the substrate (e.g., particles indicated by the blue arrow). The outline of BC aggregates was extracted using ImageJ's Frac Lac plugin (deep ImageJ) for fractal dimension calculation, which is based on the boxing counting method, for example, the image inside the blue rectangle on the lower right corner of Figure S1c.

In the boxing counting method, the theoretical basis for D_f calculation is following Eq. (4).

$$D_f = \frac{\ln N}{\ln \varepsilon} \tag{4}$$

where D_f is fractal dimension, N is the number of the primary monomers of the aggregate, ε is the scale factor relating to the radius of gyration, the average radius of the monomer and fractal prefactor (Sorensen and Roberts, 1997).

Lacunarity measures gap and heterogeneity to complement fractal dimensions in describing complexity. It uses box mass instead of box count as mentioned in the Fraclac guidelines in the ImageJ software. The Fraclac calculates L from the pixel distribution in the TEM binary image.

Figure S1. Example images of the single particle analysis using ImageJ's plugin: (a) Before beam focus in the TEM image, (b) particles marked with numbers in yellow using ImageJ, and (c) after beam focus in the TEM image.

3. Meteorological data for single particle sampling during navigation and stop

The time series of ship heading, relative wind direction (RWD), and relative wind speed (RWS) with a 3-sec time resolution in the South China Sea during the campaign (May 05–June 09, 2021) is shown in Figure S2. The RWD and RWS varied considerably and frequently due to the operational starts and stops (halts) of the ship for other tasks. The 10-min averaged RWD and RWS data were determined based on vector calculations. Detailed meteorological data, encompassing the 10-min average for single particle sampling during navigation and stop, are listed in Table S1. The sampling location for single particle sampling is shown in Figure S3.

Note that the samples collected during navigation were free from interference from the own ship emission due to high relative wind speeds (>5 m s^{-1}) and appropriate relative wind directions (0°–80°, 280°–360°). Samples collected with wind speeds below 5 m s^{-1} or at relative wind direction in the range of 80°–280° were air masses mixed with the own ship emissions.

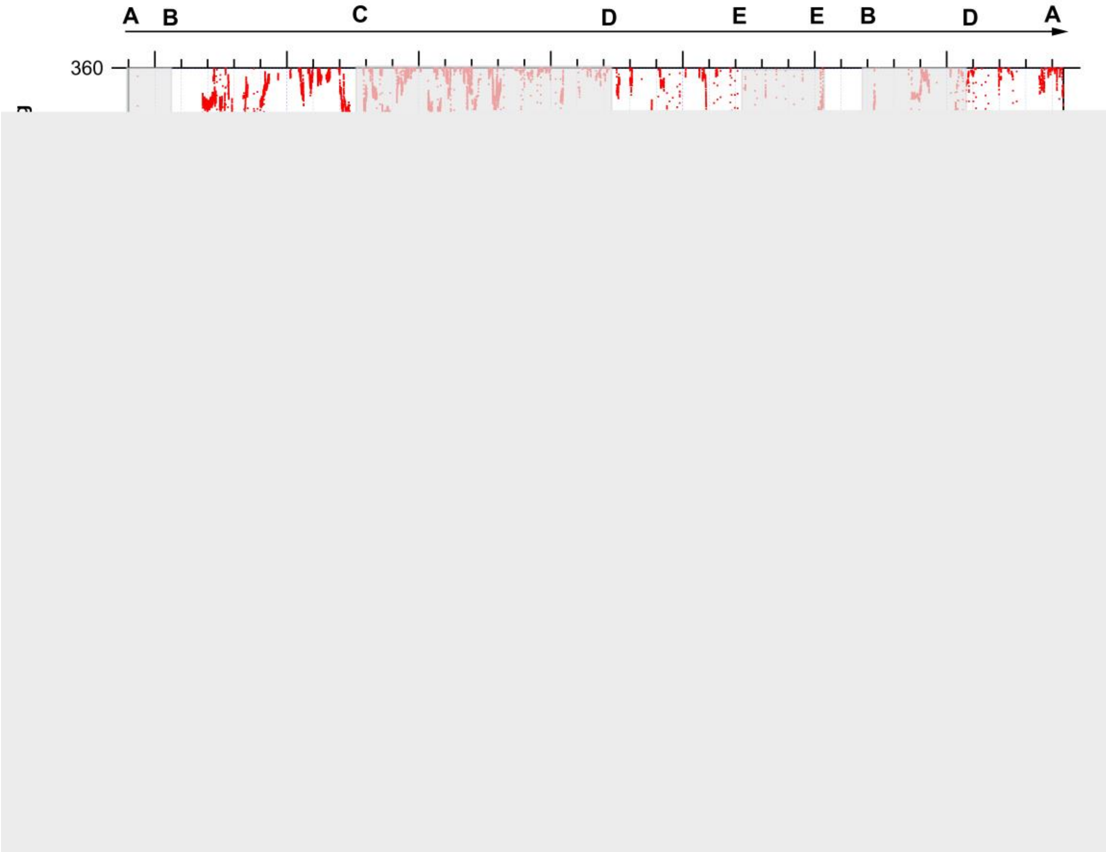

Figure S2. Time series of ship heading, relative wind direction (RWD), and relative wind speed (RWS) during the campaign in the South China Sea (SCS). The shaded and unshaded areas sequentially indicate the cruise routes from A to B, B to C, C to D, D to E, E (ship stop), E to B, B to D, and D to A, as marked in Figure 1 in the main text.

Table S1. Meteorological data on the 10-min average single particle sampling during navigation and stop.

Serial number	Sampling start time	P (hPa)	RH (%)	S.R. (W m^{-2})	Temp. (°C)	RWS* (m s^{-1})	RWD* (°)
N1	2021/5/10 11:18	1008.3 ± 0.0	81.0 ± 0.7	961.9 ± 42.4	29.7 ± 0.0	10.5 ± 0.6	341.7 ± 50.7
N2	2021/5/11 8:24	1007.9 ± 0.0	83.3 ± 0.5	491.6 ± 10.1	28.9 ± 0.1	9.8 ± 0.5	320.2 ± 46.7
N3	2021/5/11 19:00	1006.6 ± 0.1	75.5 ± 0.5	-	29.7 ± 0.0	6.4 ± 0.8	336.1 ± 21.1
N4	2021/5/12 8:13	1007.5 ± 0.1	78.8 ± 0.6	474.5 ± 32.9	29.4 ± 0.1	7.0 ± 0.4	327.7 ± 53.1
N5	2021/5/15 19:15	1006.6 ± 0.0	77.8 ± 1.9	-	30.2 ± 0.1	6.2 ± 0.7	60.1 ± 37.2
N6	2021/5/16 12:35	1007.5 ± 0.0	76.9 ± 0.7	989.8 ± 13.2	29.8 ± 0.0	10.8 ± 0.7	340.3 ± 59.0
N7	2021/5/17 14:40	1006.6 ± 0.0	72.2 ± 0.9	758.7 ± 7.7	30.0 ± 0.0	10.0 ± 0.6	16.9 ± 47.7
N8	2021/5/18 8:47	1009.3 ± 0.0	79.3 ± 0.5	647.1 ± 68.5	30.1 ± 0.0	7.3 ± 0.5	12.3 ± 59.7

N9	2021/5/18 18:10	1007.0 ± 0.0	75.8 ± 0.4	28.5 ± 6.1	30.7 ± 0.0	5.3 ± 0.4	14.2 ± 50.4
N10	2021/5/21 16:16	1006.2 ± 0.1	74.0 ± 0.5	244.8 ± 62.2	30.2 ± 0.0	6.0 ± 1.2	16.8 ± 29.5
N11	2021/5/22 15:32	1005.3 ± 0.0	82.1 ± 0.7	551.3 ± 140.5	28.5 ± 0.1	6.3 ± 1.0	57.4 ± 19.6
N12	2021/5/27 8:55	1009.2 ± 0.0	76.1 ± 0.7	666.6 ± 16.4	29.8 ± 0.1	7.0 ± 0.4	291.8 ± 45.9
N13	2021/6/1 18:07	1004.7 ± 0.0	76.1 ± 0.3	78.6 ± 14.6	30.3 ± 0.0	8.0 ± 0.5	40.0 ± 45.2
N14	2021/6/3 10:50	1005.4 ± 0.1	77.9 ± 0.7	151.9 ± 6.7	30.1 ± 0.0	10.1 ± 0.5	313.2 ± 61.3
N15	2021/6/8 10:18	1008.8 ± 0.0	86.2 ± 0.4	259.7 ± 40.5	28.4 ± 0.1	5.1 ± 0.7	58.6 ± 19.7
S1	2021/5/9 14:36	1007.2 ± 0.0	74.6 ± 0.5	739.4 ± 164.0	29.4 ± 0.1	1.8 ± 0.7	242.4 ± 62.3
S2	2021/5/9 15:30	1006.6 ± 0.1	75.3 ± 0.8	686.9 ± 32.3	29.5 ± 0.2	3.0 ± 0.6	238.5 ± 42.3
S3	2021/5/13 9:07	1006.6 ± 0.0	77.1 ± 0.6	709.6 ± 12.6	30.4 ± 0.0	0.1 ± 1.3	222.1 ± 32.9
S4	2021/5/13 19:15	1005.8 ± 0.0	65.0 ± 1.4	-	30.4 ± 0.1	5.5 ± 2.1	95.9 ± 67.1
S5	2021/5/14 10:50	1006.9 ± 0.0	75.4 ± 0.5	932.7 ± 4.1	30.9 ± 0.1	2.4 ± 0.7	193.3 ± 38.7
S6	2021/5/16 21:50	1008.3 ± 0.1	77.3 ± 0.8	-	29.8 ± 0.1	3.7 ± 0.5	68.3 ± 48.3
S7	2021/5/18 21:12	1008.0 ± 0.0	77.0 ± 0.0	-	30.5 ± 0.0	0.5 ± 0.4	128.1 ± 51.4
S8	2021/5/19 8:42	1008.2 ± 0.0	74.8 ± 0.6	661.4 ± 6.3	31.0 ± 0.1	2.1 ± 0.6	123.0 ± 32.5
S9	2021/5/20 18:00	1007.7 ± 0.1	68.5 ± 0.5	54.4 ± 8.6	31.6 ± 0.1	0.3 ± 0.3	109.5 ± 40.4
S10	2021/5/22 8:40	1008.0 ± 0.1	73.8 ± 0.6	278.1 ± 136.2	30.2 ± 0.1	1.3 ± 0.3	43.1 ± 66.1
S11	2021/5/23 8:39	1007.6 ± 0.1	74.9 ± 0.7	646.7 ± 9.9	30.1 ± 0.1	3.2 ± 0.6	83.0 ± 61.8
S12	2021/5/23 20:43	1008.6 ± 0.0	80.4 ± 0.7	-	29.1 ± 0.1	3.6 ± 0.6	91.5 ± 69.4
S13	2021/5/24 8:01	1009.3 ± 0.0	74.9 ± 0.3	526.1 ± 10.5	30.3 ± 0.1	2.5 ± 0.5	133.4 ± 43.6
S14	2021/5/24 16:03	1007.1 ± 0.0	75.7 ± 0.8	94.5 ± 4.9	30.4 ± 0.1	2.4 ± 0.7	76.9 ± 48.1
S15	2021/5/25 9:21	1010.1 ± 0.0	77.6 ± 0.5	734.1 ± 86.0	29.8 ± 0.1	4.7 ± 0.5	317.3 ± 47.0
S16	2021/5/30 22:11	1002.9 ± 0.1	96.0 ± 0.0	-	27.3 ± 0.0	2.0 ± 0.3	108.9 ± 68.7
S17	2021/6/2 9:10	1007.2 ± 0.0	78.5 ± 0.5	675.9 ± 17.1	29.8 ± 0.1	3.1 ± 0.4	17.6 ± 42.1
S18	2021/6/5 18:23	1003.0 ± 0.1	83.8 ± 0.4	2.3 ± 0.5	29.0 ± 0.1	11.8 ± 0.9	279.0 ± 36.0
S19	2021/6/7 8:45	1006.7 ± 0.1	86.3 ± 0.9	110.9 ± 36.6	27.8 ± 0.1	4.1 ± 3.2	105.5 ± 45.3

* The relative wind direction and wind speed are 10-min vector average.

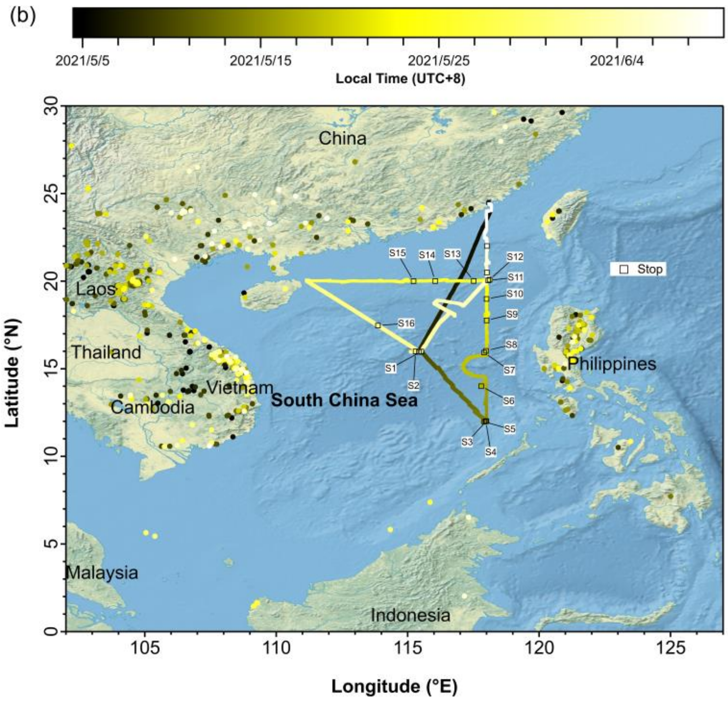

Figure S3. Map of the ship route in the South China Sea during the campaign. The open triangles in (a) and squares in (b) indicate the single particle sampling location, collected during navigation and stop. The samples marked in N1 to N15 for navigation sampling and S1 to S19 for stop sampling in serial. The solid circles indicate the fire spots with a confidence level greater than 80% using MODIS satellite data.

4. AAE calculation

The long-range biomass burning transport affects the air mass in the South China Sea (SCS). Two methods were used to obtain the hourly absorption Ångström exponent (AAE) values from the AE33 measurements. Figure S4a shows an example of the AAE calculation for a ship plume at 18:00 on May 5. Figure S4b demonstrates the linear relationship between the AAE values obtained from all wavelengths and those obtained from a pair of wavelengths at 470 and 950 nm. The fitting results indicate that AAE (all wavelengths) was lower than AAE (470, 950 nm) with a fitting slope of 0.78 and a determination coefficient (R^2) of 0.98.

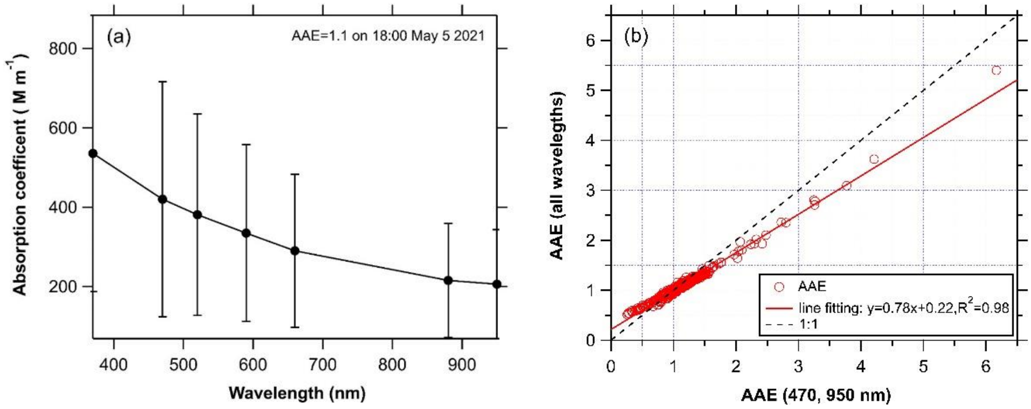

Figure S4. (a) A ship plume at 18:00 on May 05 for the wavelength-dependent absorption Angström exponent (AAE) based on the hourly averaged data, (b) AAE obtained from all the wavelengths vs the AAE obtained from two wavelengths at 470 and 950 nm based on hourly averaged data during the campaign.

5. Typhoon 202103 (CHOI-WAN)

Typhoon 202103 (CHOI-WAN) was born on 18:00 UTC, May 30, 2021, and dead on 6:00 UTC, June 5, 2021. We met this typhoon during our cruise measurement. Figure S5 shows the best track of the map and central pressure chart. Basic information is available online (http://agora.ex.nii.ac.jp/digital-typhoon/summary/wnp/s/202103.html.en).

(a)

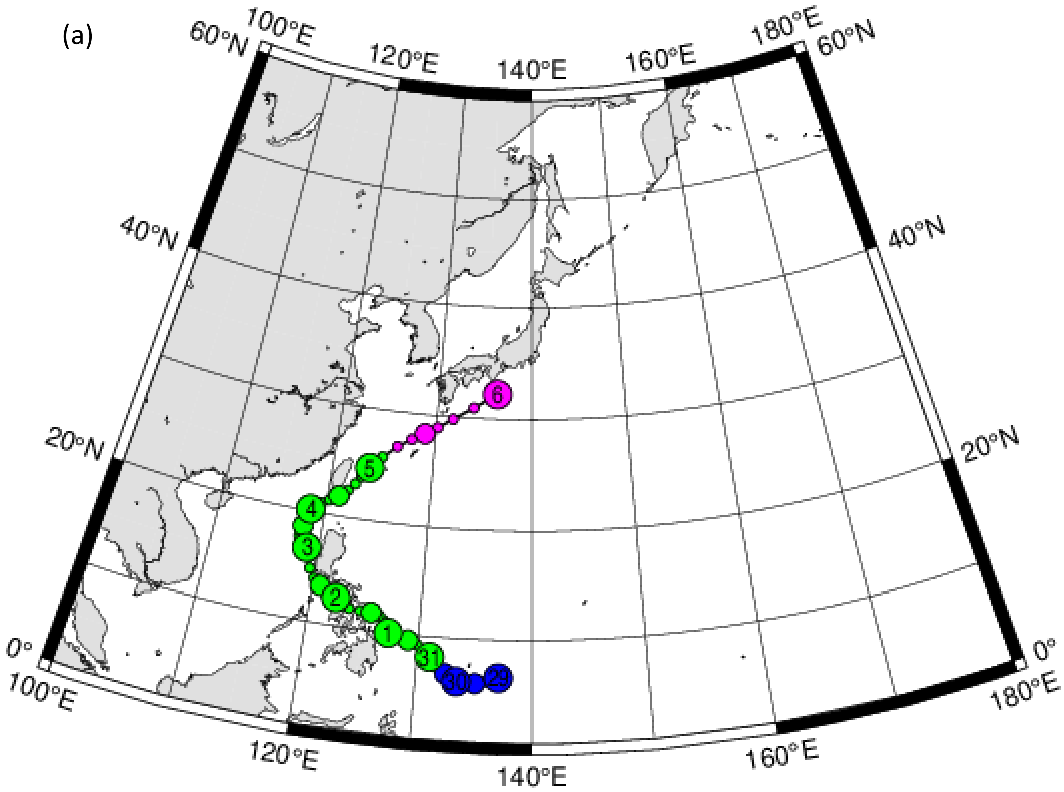

(b)

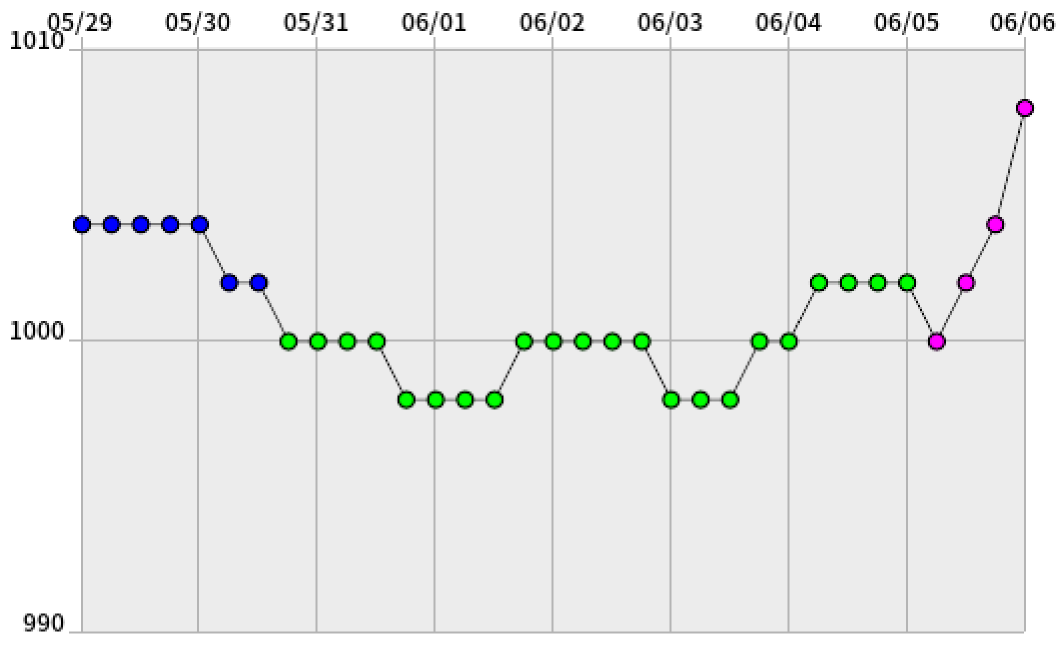

Figure S5. (a) Best track map of the typhoon 202103 (CHOI-WAN), and (b) the central pressure chart (time zone=UTC, Local time=UTC+8).

6. Multi-peak fitting of single particles

We didn't successfully obtain a bimodal or multi-peak fit for data of the stop cases using the multi-peak fitting function in Igor Pro software, as shown in Figure S15-6.

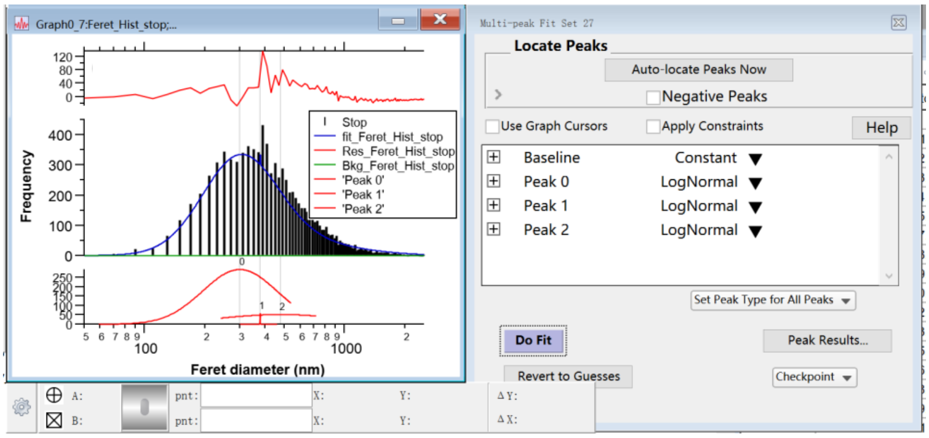

Figure S6. Multi-peak fit particle size distribution using Feret diameter determined with Igor Pro software during stop (b).

7. TEM images and EDS spectrum of the BC particles and the tar balls

Figure S7 shows the TEM images of the three Navigation samples before and after beam focus, revealing the presence of external and internal BC particles. Figure S8 presents the representative single particles and their corresponding EDS spectra for the navigation samples, indicating that the major components are: (a, c) BC and sulfate, (b) sulfate, (d) sea salt, organics and BC. Notably, detecting nitrogen (N) element in EDS is challenging due to its high vaporization rate, whereas potassium (K) serves as a tracer for biomass-burning in the BC- and sulfate-containing particles.

The stop samples, shown in Figure S9, exhibit both internal mixtures and externally large aggregates of the BC particles. The EDS point analysis of freshly emitted BC particles in Figure S9c reveals the presence of very thin coating elements. In summary, the stop single particles were influenced by both the own ship emissions and long-range transport air masses.

Figure S10 depicts example images of tar balls mixed with black carbon in the geometrical size range of 159–190 nm from the single particles collected during stop on May 14 and 23, 2021. The backward trajectories suggest that the air masses were originated from the Philippines, possibly due to biomass burning during those days. Figure S11 shows example images of pure BC particles, consisting of nano-soot particles with a diameter of 40–50 nm. Obviously, the size of tar balls is significantly larger than that of nano-soot spheres.

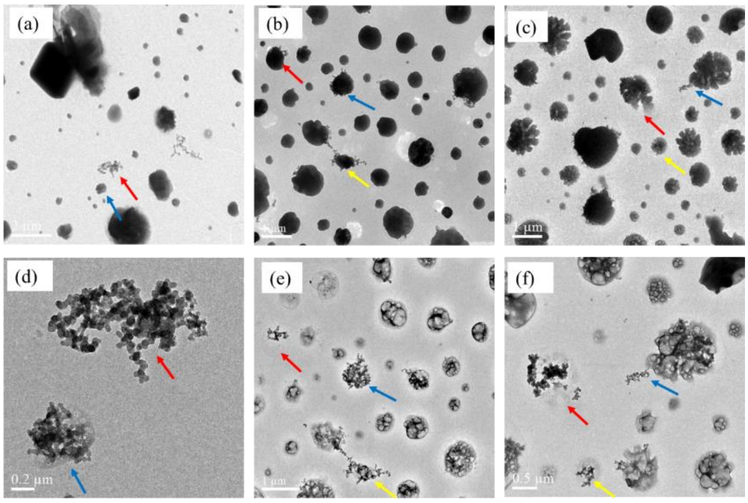

Figure S7. The example TEM images before (a, b, and c) and after (d, e and f) electron beam focus for the single particles collected during navigation. The same color arrows in each pair of images (a and d, b and e, c and f) indicate the same single particles.

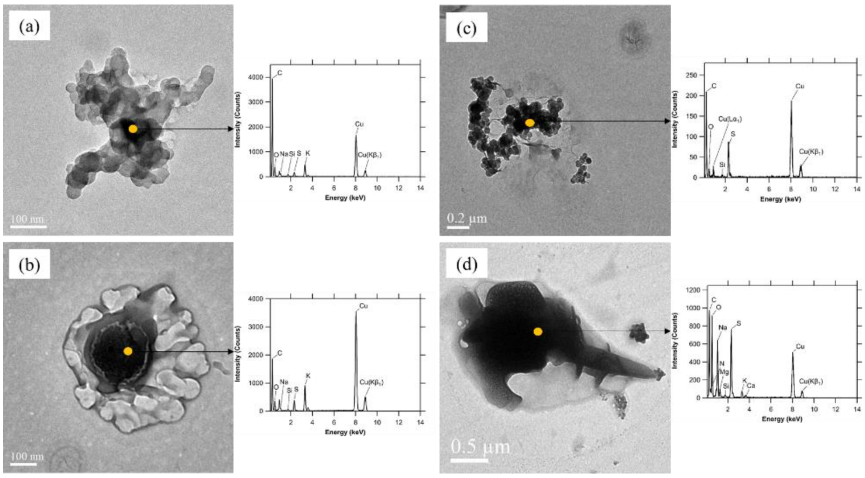

Figure S8. Examples of the EDS spectra for the single particles from the navigation samples. Si and Cu are excluded from the particle composition. (a) BC, and thin sulfate coating (Na_2SO_4, K_2SO_4), (b) sulfate (Na_2SO_4, K_2SO_4), (c) BC, and thick sulfate coating, and (d) BC, sea salt. The orange spots indicate the point analysis of EDS spectra. The right spectrum corresponds to each left particle. The Y-axis is the intensity (counts) and X-axis is the energy (KeV).

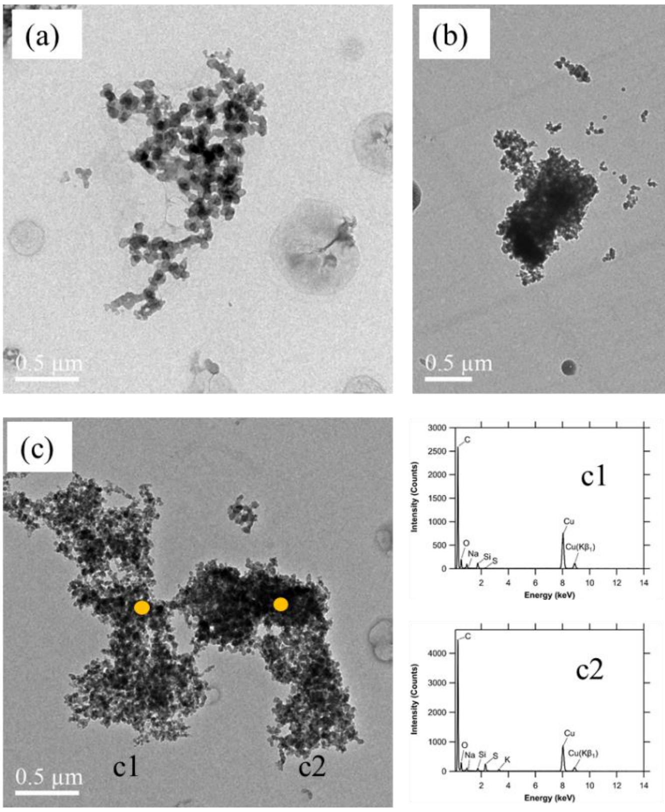

Figure S9. The example TEM images (a, b, c) of BC particles collected during stop. The orange spots indicated the point analysis of the EDS spectra (the left part c1 and the right part c2) are for the image c.

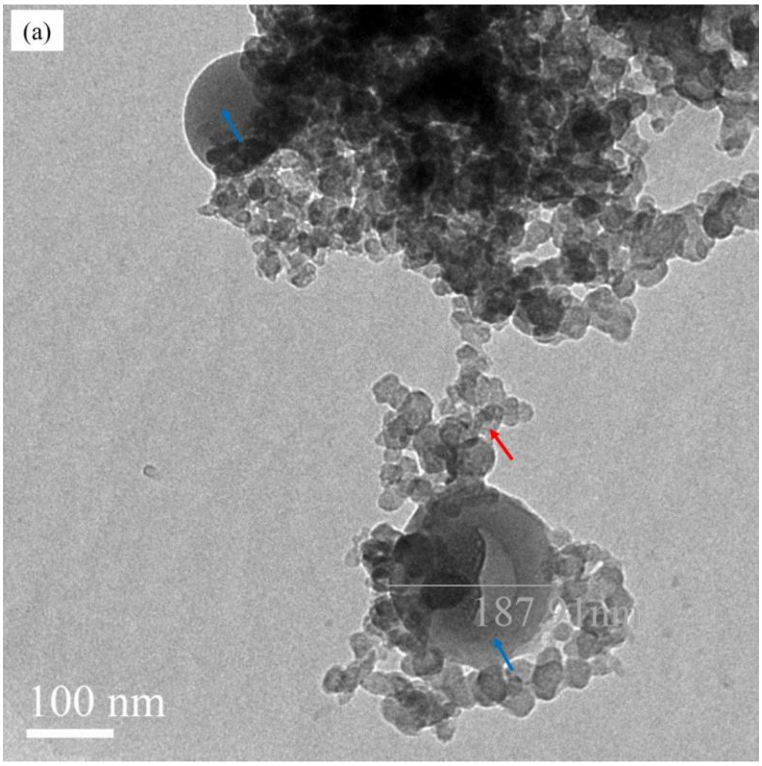

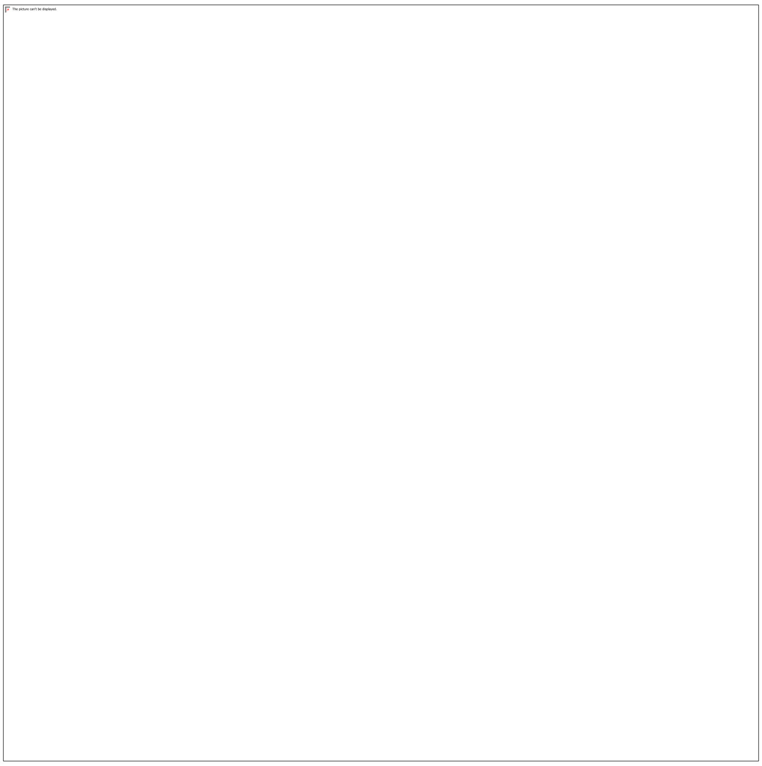

Figure S10. Example images of tar ball-containing particles collected during stop: (a) tar balls (170–190 nm) mixed with black carbon (BC) and sea salt on 10:50 May 14 2021; (b) tar balls consisting of 159 nm spherical particles on 8:39 May 23, 2021. The red arrows indicated BC particles and the blue arrows indicated tar balls.

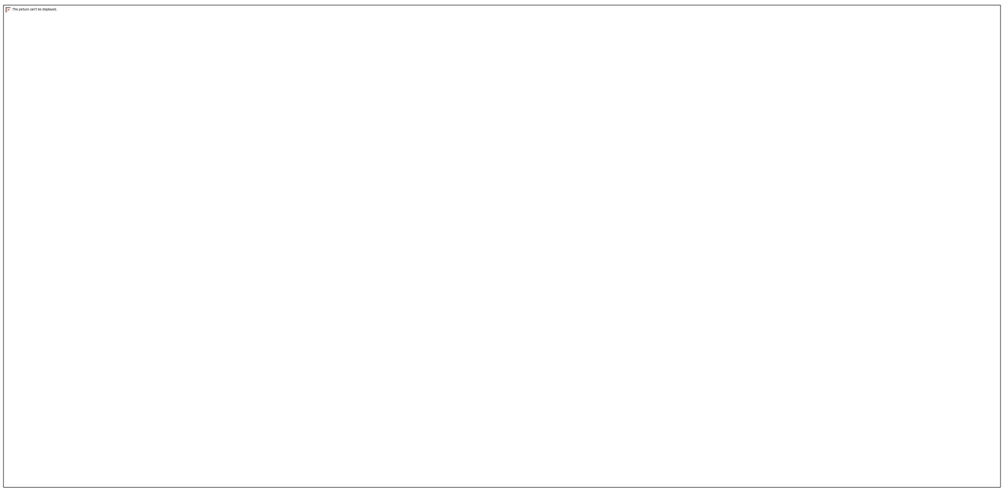

Figure S11. Images of (a) aggregated BC particles, (b) BC made of small 40–50 nm nano-soot spheres. The S11(b) image is a magnification of the part in the red rectangle in panel a.

8. The diurnal average variation of OC, EC

Figure S12(a, b) shows the linear relationship between the Magee AE33 derived BC at 880 nm and the Sunset derived optical EC at 660 nm, with a time resolution of 1 min and 1h, respectively. The limit of detection (LOD) for optical EC, as determined by the Sunset OC/EC analyzer, is 0.062 µg C m^{-3}, based on the blank filter analysis of three times the standard deviation (3σ). The fitted correlation between the two variables in Figure S12a has a slope and intercept of the 0.97 and 0.44, respectively, with a determination coefficient (R^2) of 0.68. However, the linear correlation between the AE33 derived BC and the Sunset EC at a time resolution of 1 h has a slope and intercept of 1.66 and -0.01, respectively, with a higher R^2 of 0.91 (Figure S12b). In addition, Figure S12c displays the correlation between the optical EC and thermal EC data measured by the Sunset instrument. The slope and intercept of the fitted line are 1.55 and -0.21, respectively, with R^2=0.97. The differences of the two instruments are mainly attributed to the technical principles of the methods used for the data processing. Similar results have been reported in other studies (Brown et al., 2019).

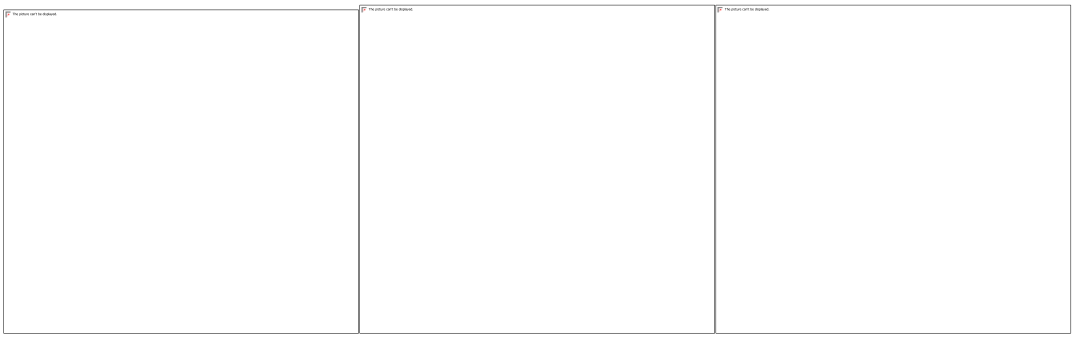

Figure S12. The linear relationship between the AE33 derived BC and the Sunset derived optical EC with 1-min time resolution (a), thermal EC with 1-h time resolution (b), and Sunset derived optical EC vs thermal EC with 1-h time resolution (c) for all the data during the campaign in the SCS.

9. Possible biological particles collected during the campaign

Two examples of possible biological particles were collected on two different days. Figure S13a displays brocosomes, which are known to be produced by leaf-hopping insects. This finding is supported by a previous study (Fu et al., 2012). Figure S13b depicts a rod-like particle that has yet to be identified.

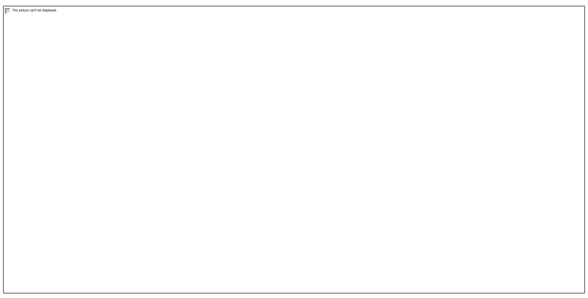

Figure S13. (a) Flower-like biological particles collected at 10:50 on May 14, (b) Rod-like biological particles collected at 8:01 on May 24.

10. CALIPSO observation

Cloud-Aerosol Lidar & Infrared Satellite Observation (CALIPSO) is a remote sensor on board the TERRA and AQUA satellites. CALIPSO observation can provide vertical and horizontal distribution of the cloud and aerosol layers using the elastic backscatter intensities (extinction-to-backscatter ratio) at an Nd:YAG laser wavelength of 532 and 1064 nm near the nadir of the orbit track. CALIPSO L1 Standard V4.20 products are available from the NASA Langley Research Center (https://www-calipso.larc.nasa.gov/tools/data_avail/). Images of vertical feature mask (VFM) and aerosol subtype (AS) were used to show the vertical and horizontal properties of clouds, aerosol layer and identification (Liu et al., 2019; Omar et al., 2009). Convective transport is important to the vertical distribution of aerosols (Niu et al., 2019).

Figures S14 and S15 show the orbit track location, vertical feature mask, and aerosol subtype at 6:00 on May 15, and 19:30 on June 07, respectively. These images show that polluted continental/smoke and elevated smoke exist in the aerosol layer with an altitude of 1–3 km over the SCS regions and Southeast Asia.

Figure S14. (a) Orbit track location indicated by blue curve, (b) vertical feature mask, and (c) aerosol subtype at UTC 6:00 on May 15, a time before the summer monsoon started in the SCS.

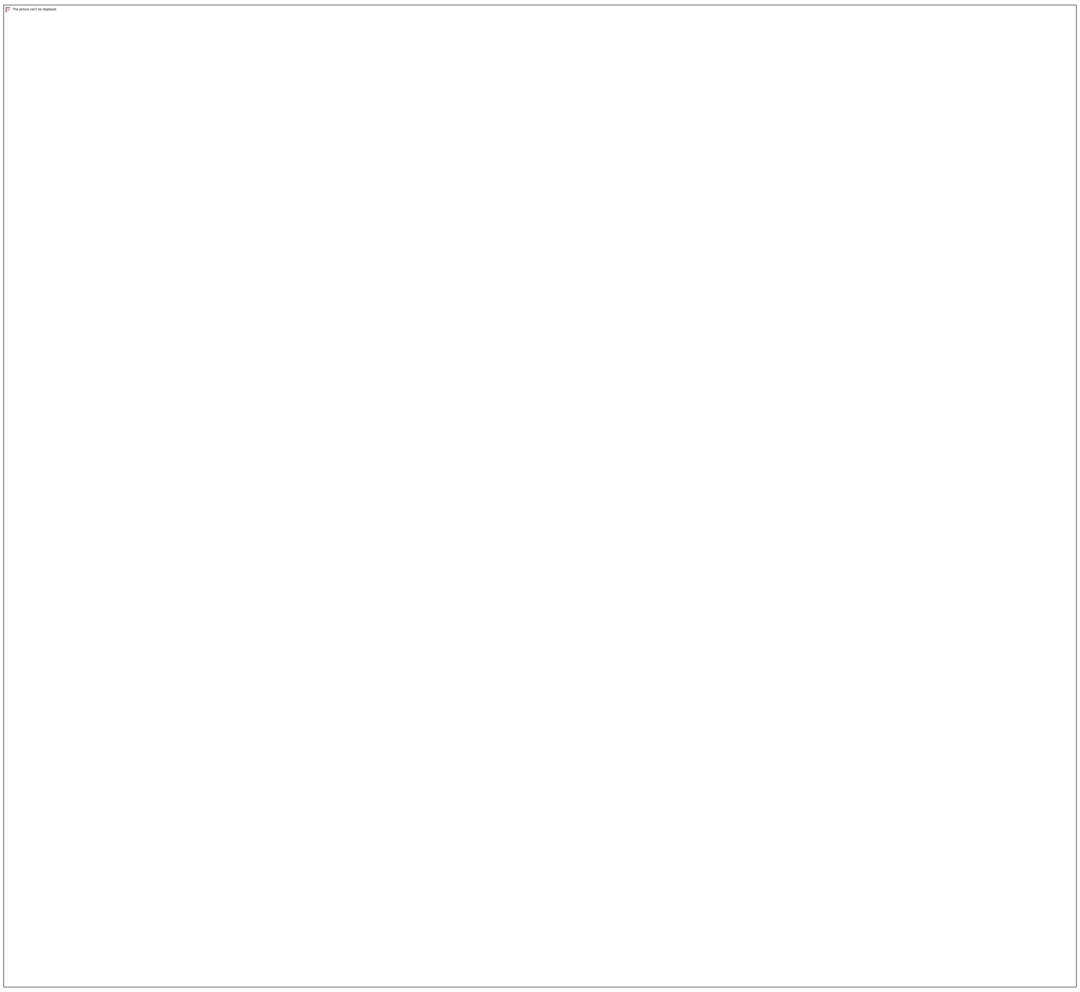

Figure S15. (a) Orbit track location indicated by blue curve, (b) vertical feature mask, and (c) aerosol subtype at UTC 19:30 on June 07, a time after summer monsoon passed in the SCS.

11. Time resolution and accuracy for the automatic weather station

The time resolutions for the original meteorological and GPS data are 3 seconds. The position accuracies for the X and Y axes are 1 cm +1 ppm RMS (root mean square), and for Z axis is 2 cm +1 ppm RMS. The accuracy of wind speed and wind direction is ± 0.2 m s-1 (or 3% of reading) and ± 2°, respectively. The accuracy of temperature with RS-485 output at +20 to +60 °C is ± (0.07 + 0.0025 × temperature) °C. The accuracy of relative humidity at -20 to + 40 °C is ± (1 + 0.008 ×reading) %RH. The accuracy of pressure with factory calibration is ± 0.15 hPa (Class A).

12. Additional BC fractal analysis

A combination of BC particles in this study collected in the South China Sea and previous BC particles collected on an island in the East China Sea (Sun et al, 2020) is shown in Figure S16.

Figure S16. The size-dependent fractal dimension (D_f) and lacunarity (L) for each BC particle during navigation and stop. A total number of 240 data points are shown in Figure S16. LRT and indicated particles from long-range transport and local pollution, respectively.

References

Brown, S., Minor, H., O'Brien, T., Hameed, Y., Feenstra, B., Kuebler, D., Wetherell, W., Day, R., Tun, R., Landis, E., and Rice, J.: Review of Sunset OC/EC instrument measurements during the EPA's Sunset carbon evaluation project, Atmosphere (Basel), 10, 287, https://doi.org/10.3390/atmos10050287, 2019.

Fu, H., Zhang, M., Li, W., Chen, J., Wang, L., Quan, X., and Wang, W.: Morphology, composition and mixing state of individual carbonaceous aerosol in urban Shanghai, Atmos. Chem. Phys., 12, 693–707, https://doi.org/10.5194/acp-12-693-2012, 2012.

Liu, Y., Zhu, Q., Wang, R., Xiao, K., and Cha, P.: Distribution, source and transport of the aerosols over Central Asia, Atmos. Environ., 210, 120–131, https://doi.org/10.1016/j.atmosenv.2019.04.052, 2019.

Marple, V. A. and Olson, B. A.: Sampling and measurement using inertial, gravitational, centrifugal, and thermal techniques, in: Aerosol measurement: Principles, techniques, and applications, edited by: Kulkarni, P., Baron, P. A., and Willeke, K., John Wiley and Sons, Hoboken, New Jersey, USA, 129–151, https://doi.org/10.1002/9781118001684.ch8, 2011.

Niu, H., Kang, S., Gao, W., Wang, Y., and Paudyal, R.: Vertical distribution of the Asian tropopause aerosols detected by CALIPSO, Environ. Pollut., 253, 207–220, https://doi.org/10.1016/j.envpol.2019.06.111, 2019.

Omar, A. H., Winker, D. M., Vaughan, M. A., Hu, Y., Trepte, C. R., Ferrare, R. A., Lee, K.-P., Hostetler, C. A., Kittaka, C., Rogers, R. R., Kuehn, R. E., and Liu, Z.: The CALIPSO automated aerosol classification and Lidar ratio selection algorithm, J. Atmos. Ocean. Technol., 26, 1994–2014, https://doi.org/10.1175/2009jtecha1231.1, 2009.

Sorensen, C. M. and Roberts, G. C.: The Prefactor of Fractal Aggregates, J. Colloid. Interf. Sci., 186, 447-452, https://doi.org/10.1006/jcis.1996.4664, 1997.

Sun, C., Adachi, K., Misawa, K., Cheung, H. C., Chou, C. C. K., and Takegawa, N.: Mixing state of black carbon particles in Asian outflow observed at a remote site in Taiwan in the spring of 2017, J. Geophys. Res. Atmos., 125, 13, https://doi.org/10.1029/2020jd032526, 2020.

Zhang, K., Allen, G., Yang, B., Chen, G., Gu, J., Schwab, J. J., Felton, D., and Rattigan, O.: Joint measurements of PM2. 5 and light-absorptive PM in woodsmoke-dominated ambient and plume environments, Atmos. Chem. Phys., 17, 11441–11452, https://doi.org/10.5194/acp-17-11441-2017, 2017.